Bulletin of the Seismological Society of America, Vol. 103, No. 1, pp. 353–370, February 2013, doi: 10.1785/0120120108

Rupture History of the 2008 M_w 7.9 Wenchuan, China, Earthquake: Evaluation of Separate and Joint Inversions of Geodetic, Teleseismic, and Strong-Motion Data

by Stephen Hartzell, Carlos Mendoza, Leonardo Ramirez-Guzman,
Yuehua Zeng, and Walter Mooney

Abstract An extensive data set of teleseismic and strong-motion waveforms and geodetic offsets is used to study the rupture history of the 2008 Wenchuan, China, earthquake. A linear multiple-time-window approach is used to parameterize the rupture. Because of the complexity of the Wenchuan faulting, three separate planes are used to represent the rupturing surfaces. This earthquake clearly demonstrates the strengths and limitations of geodetic, teleseismic, and strong-motion data sets. Geodetic data (static offsets) are valuable for determining the distribution of shallower slip but are insensitive to deeper faulting and reveal nothing about the timing of slip. Teleseismic data in the distance range 30°–90° generally involve no modeling difficulties because of simple ray paths and can distinguish shallow from deep slip. Teleseismic data, however, cannot distinguish between different slip scenarios when multiple fault planes are involved because steep takeoff angles lead to ambiguity in timing. Local strong-motion data, on the other hand, are ideal for determining the direction of rupture from directivity but can easily be over modeled with inaccurate Green's functions, leading to misinterpretation of the slip distribution. We show that all three data sets are required to give an accurate description of the Wenchuan rupture. The moment is estimated to be approximately $1.0 \times 10^{21}\ \mathrm{N \cdot m}$ with the slip characterized by multiple large patches with slips up to 10 m. Rupture initiates on the southern end of the Pengguan fault and proceeds unilaterally to the northeast. Upon reaching the cross-cutting Xiaoyudong fault, rupture of the adjacent Beichuan fault starts at this juncture and proceeds bilaterally to the northeast and southwest.

Introduction

The 12 May 2008 M_w 7.9 Wenchuan, China, earthquake was a devastating event in terms of ground shaking and subsequent landslides, resulting in great loss of life (Dai *et al.*, 2011). Surface breaks occurred over a 240-km length of the Longmen Shan fault zone in the predominantly convergent zone with right-lateral motion separating the Sichuan basin to the east from the eastern margin of the Tibetan plateau (Fig. 1). Detailed mapping of the surface faulting has revealed the rupture of two northwest-dipping imbricate oblique reverse faults: the Beichuan fault, the main fault involved in the Wenchuan earthquake, and the Pengguan fault lying approximately 12 km to the east along the range front (Xu *et al.*, 2009; Densmore *et al.*, 2010; Liu-Zeng *et al.*, 2010; Yu *et al.*, 2010). In addition, the Xiaoyudong fault, a short tear fault striking nearly perpendicular to the Beichuan and Pengguan faults, links these two faults near the southern end of the mapped surface rupture. Seismic, geologic, and gravimetric data have been used to construct 3D fault and velocity models of the region (Hubbard *et al.*, 2010; Gardner *et al.*, 2011).

Several studies have been made of the source of the Wenchuan earthquake using different data sets. Several of these studies have been done using geodetic data, Global Positioning System (GPS) or Interferometric Synthetic Aperture Radar (InSAR) (Shen *et al.*, 2009; Feng *et al.*, 2010; Furuya *et al.*, 2010; Xu *et al.*, 2010). Other studies have considered the teleseismic waveforms (Ji and Hayes, 2008, see Data and Resources; Nishimura and Yagi, 2008, see Data and Resources; Zhang and Ge, 2010). In addition, Shao *et al.* (2010) used geodetic, teleseismic, and strong-motion data with a nonlinear inversion method to obtain the slip history. In this study we also use all three of these data sets but with a linear time-window approach to the source parameterization. We also investigate the strengths and limitations of each of these data sets and the importance of including geodetic, teleseismic, and strong-motion data to

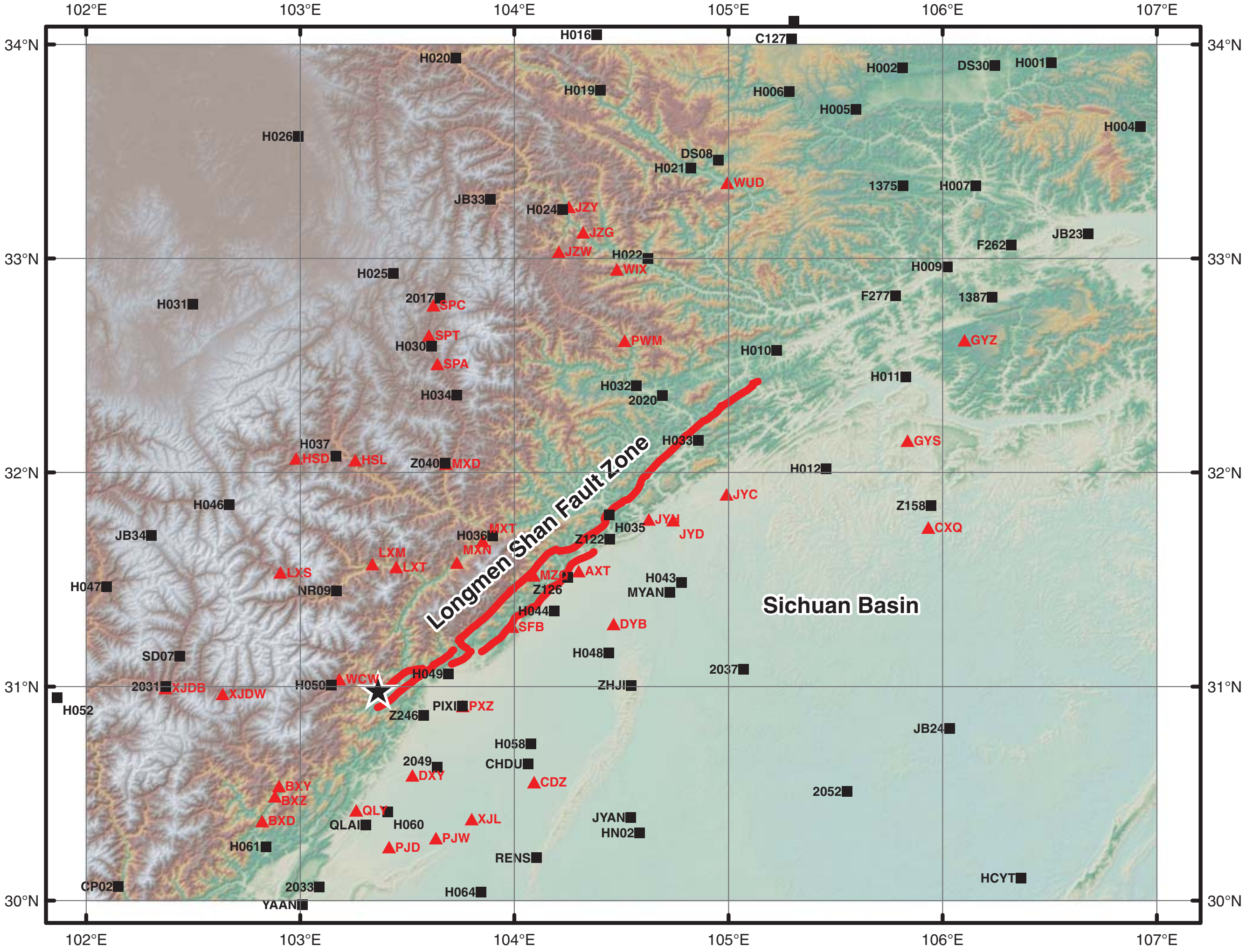

Figure 1. Region of the Wenchuan earthquake at the western edge of the Sichuan basin and the eastern margin of the Tibetan plateau. Mapped surface rupture along the Longman Shan fault zone, bold red; geodetic stations, black squares; strong-motion stations, red triangles; hypocenter, star.

obtain a complete picture of the rupture. Other studies have used slip distributions obtained by one or more previous investigations of the source to calculate various parameters of the local ground motion (Wei *et al.*, 2008; Bjerrum *et al.*, 2010; Chavez *et al.*, 2010; Ghasemi *et al.*, 2010; Kurahashi and Irikura, 2010).

Data

Three different data sets are used in this study: geodetic, teleseismic, and strong motion. The strengths and weaknesses of these different data are particularly revealed by the Wenchuan earthquake and is one of the primary considerations of this paper. The GPS data are from the Working Group of the Crustal Motion Observation Network of China Project (WGCMONCP; 2008) using data collected before and after the earthquake and processed by Shen *et al.* (2009). Shen *et al.* (2009) conclude that only small amounts of postseismic deformation are included in the surface displacement measurements. The postseismic deformation is estimated to be just a few percent of the coseismic from continuous GPS time series recorded during the entire postseismic period at permanent sites. Because most of the GPS sites have years of preevent occupation history, secular deformation before the earthquake was readily estimated and removed. The locations of the 117 GPS stations used in our inversion are shown in Figure 1.

Fifty broadband *P* waveforms make up the teleseismic data set. The stations lie in the distance range from 31° to 93° (Table 1). The records are all ground displacement bandpass filtered from 1 to 60 s with a time step of 0.2 s. Figure 2 shows the azimuthal coverage of the stations. The station distribution gives uniform coverage around the source, which is important for unbiased imaging of the rupture. We will further examine the station distribution in Results.

Our third data set comprises the strong-motion records from 40 stations. The locations are also shown in Figure 1. Original digital accelerations were obtained from the

Table 1
Teleseismic Stations

Station	Distance (°)	Azimuth
DAV	31.60	134.26
PALK	31.72	−133.36
BRVK	32.56	−37.74
YAK	35.44	21.13
ABKT	37.65	−66.82
KAPI	39.07	153.52
ARU	40.14	−37.39
TIXI	42.98	11.55
COCO	43.38	−170.68
PET	45.28	44.34
GNI	47.80	−62.06
DGAR	48.31	−136.98
KIV	48.85	−56.75
BILL	51.63	25.30
OBN	52.14	−41.98
LVZ	53.69	−25.95
MBWA	54.17	161.07
KEV	56.58	−23.91
WAKE	57.80	85.63
MSEY	57.82	−119.12
PMG	58.09	126.44
WRAB	58.73	145.47
KBS	60.10	−12.89
ADK	60.34	44.62
FURI	63.79	−95.40
NWAO	64.90	167.13
CTAO	65.38	135.28
KONO	65.63	−33.80
ALE	66.51	−2.02
MIDW	67.54	69.76
GRFO	68.37	−44.28
COLA	69.80	25.51
KMBO	70.26	−103.78
BFO	70.65	−44.79
KDAK	71.29	33.28
TARA	71.83	99.61
ESK	73.72	−34.80
BORG	75.34	−21.38
JOHN	79.16	77.00
SFJD	80.35	−10.07
PAB	82.95	−47.92
TAU	83.87	149.14
LSZ	85.53	−110.64
KIP	86.22	67.40
KNTN	87.05	94.97
POHA	89.06	67.57
FFC	91.89	14.38
AFI	92.73	104.48
LBTB	92.88	−117.40
COR	93.60	31.39

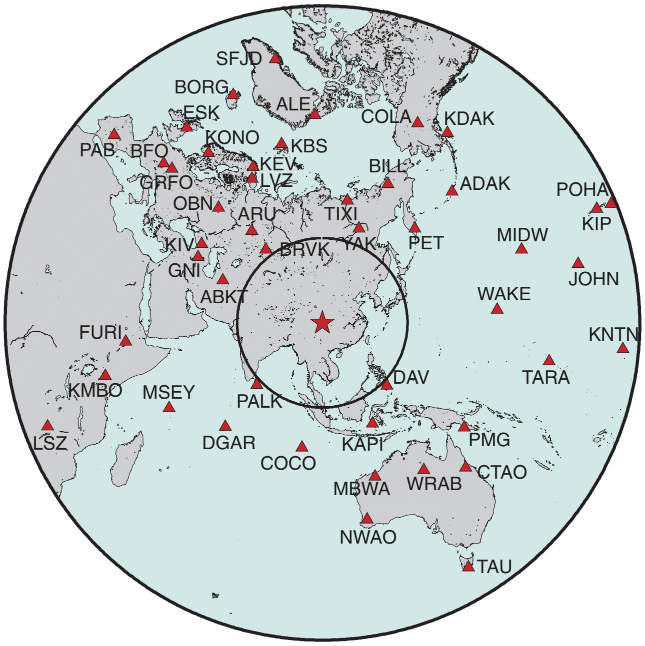

Figure 2. Distribution of teleseismic stations.

Institute of Engineering Mechanics, China Earthquake Administration, Harbin, China. We then integrated the records to ground displacement, bandpass filtered from 1 to 12.5 s with a time step of 0.2 s. The choice of displacements rather than velocities and the bandpass was made with considerable deliberation. Ground velocity records are often used in source inversion studies, but the complexity of the Wenchuan ground motion argued for the use of displacements. We tested different period bands and found the interval from 1 to 12.5 s to include the longest period with reliably stable results and the shortest period that could reasonably be modeled with our present parameterization.

Fault Model

We parameterized the complex surface rupture shown in Figure 1 using three separate fault planes: one segment for the Pengguan fault and two other segments for the southwestern and northeastern Beichuan fault. This subdivision is natural to incorporate the two subparallel Penguuan and Beichuan faults and the differences in the southwest and northeast Beichuan segments. The Penguuan segment dips at 28° and intersects the southwest Beichuan segment at a depth of 15 km. It lies approximately 12 km to the southeast at the surface from the Beichuan fault. The southwest Beichuan segment has a 43° dip and bottoms at a depth of 21 km. The northeast Beichuan segment initiates at the Gaochuan right bend at a latitude of approximately 31.6° with a dip of 50° and bottom depth of 16 km. These fault geometries were derived from the imaging and inversion results of Hubbard *et al.* (2010) and Shen *et al.* (2009). Each of the fault segments runs farther to the southwest and northeast than the mapped surface rupture to capture any hidden slip as suggested by the aftershock pattern (Zhu *et al.*, 2008). The fault parameters for each segment are summarized in Table 2, and the relative geometry of the fault segments is shown in Figure 3. We do not consider the short cross-cutting Xiaoyudong fault in the inversions because of its short length. All the fault planes extend to within 0.5 km of the surface to avoid numerical difficulties in the calculation of the wave propagation Green's functions.

Table 2

Fault Segments

Segment	Length (km)	Width (km)	Dip	Maximum Depth (km)	Subfaults (length)	Subfaults (width)
Pengguan	132	32	28	15	26	10
SW Beichuan	132	31	43	21	26	10
NE Beichuan	248	21	50	16	36	7

Method

We use the linear least-squares inversion method for kinematic fault slip of Hartzell and Heaton (1983). The approach of Hartzell and Heaton (1983) divides the fault plane into equal-area subfaults. The ground displacement for a unit amount of slip on each subfault is calculated by summing the contributions of point sources uniformly distributed over the area of the subfault with a spacing of 0.6 km. The subfault dimensions are fixed at 5.1-km long and 3-km wide for the three fault segments. The size of the subfaults is set by two competing objectives: first to make them small enough to see detail in the slip and second to make them large enough for a tractable problem. Slip is allowed to occur on each subfault in a series of discrete time intervals. The functional form of the slip rate function is assumed to be constant for each time interval and set to a 2-s boxcar. A complicated or extended rise time function, however, can be constructed on each subfault, if required by the data, by the linear combination of slips over the individual time intervals. Five time intervals are used for the Wenchuan earthquake allowing a rise time of up to 10 s on each subfault. The rupture velocity is constant at 3 km/s, with some flexibility in the timing of phases offered by the different time intervals of slip. This choice is discussed further when we introduce the teleseismic inversion. Each point source on a given subfault is delayed by the appropriate rupture time delay from the hypocenter. The rake is variable over a range of 90° by taking linear combinations of Green's functions for two different rakes (90° and 180°) at right angles on each of the subfaults. The inversion is stabilized by appending smoothing, $\mathbf{S}$, and moment minimization, $\mathbf{M}$, constraints to the least-squares problem, $\mathbf{Ax} = \mathbf{b}$, resulting in

$$\begin{pmatrix} \mathbf{C}_d^{-1}\mathbf{A} \\ \lambda_1 \mathbf{S} \\ \lambda_2 \mathbf{M} \end{pmatrix} \mathbf{x} \cong \begin{pmatrix} \mathbf{C}_d^{-1}\mathbf{b} \\ 0 \\ 0 \end{pmatrix},$$

where λ_1 and λ_2 are linear weights, the magnitudes of which control the trade-off between satisfying the constraints and fitting the data. $\mathbf{C}_d$ is an *a priori* data covariance matrix that is used as a data scaling matrix. The data covariance matrix is diagonal and normalizes each data record to peak amplitude of 1.0. Thus, each record has nearly equal weight in the inversion. An exception to this procedure is made in the case of geodetic data. For geodetic data we follow Wald and Graves (2001) and do not normalize amplitudes. The reasoning here is that even in the near-field geodetic measurements can be near zero, and normalization to a common amplitude could lead to instabilities. The solution vector $\mathbf{x}$ is obtained by using the Householder reduction method that invokes a positivity constraint on the solution (Lawson and Hanson, 1974), that is, each of the elements of the vector $\mathbf{x}$ is greater than or equal to zero. Our formulation with smoothing and minimization constraints is an example of Tikhonov regularization (Hansen, 1998). The optimum values for the constraint weights can be found from classic L-curve analysis, which plots the trade-off between the residual norm and the constraint norm for different constraint weights (Lawson and Hanson, 1974; Hansen, 1998). We use a trial-and-error approach of determining the constraint weights, increasing the values until there is degradation in the fit to the data based on the L2 norm. In most applications of our stabilization method, the same weight is used for spatial smoothing and moment minimization ($\lambda_1 = \lambda_2$), and we follow this procedure for the Wenchuan earthquake. Support for this approach is given by the fact that our constraint weight is within 10% of the value obtained by the empirical method of Mendoza and Hartzell (2012). They show that the constraint weight obtained by L-curve analysis over a wide range in magnitude is within a factor of two of the value obtained by taking 90 times the average of the absolute values of the elements of the $\mathbf{A}$ matrix, excluding constraints. Furthermore, they show that a factor of two in the constraint weight near the optimum point of the L-curve yields similar estimates of slip distribution and moment. Therefore, when using trial-and-error estimation, the empirical method of Mendoza and Hartzell (2012), or L-curve analysis, the results do not vary significantly.

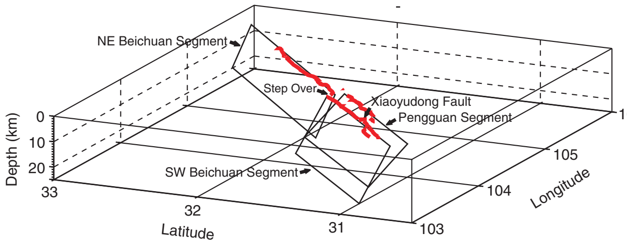

Figure 3. Fault model used to invert for the rupture history of the Wenchuan earthquake consisting of three planar surfaces: Pengguan segment, SW Beichuan segment, and NE Beichuan segment. Mapped surface rupture, bold red.

Green's functions for the GPS data are calculated using the layered half-space method of Xie and Yao (1989). Synthetics for the teleseismic problem are calculated with generalized ray theory (Helmberger, 1983). The strong ground-motion

Green's functions are based on the full wave theory frequency–wavenumber method for a layered half-space of Zhu and Rivera (2002). Because of the significant thickening of the crust moving from the Sichuan Basin across the Longmen Shan fault zone and into Tibet, and because of the existence of a distinct low velocity zone on the Tibet side of the fault (Li *et al.*, 2010), two different 1D velocity models are used for the northwestern and southeastern sides of the fault. The velocity models are given in Table 3 (C. Ji, personal commun, 2011).

Table 3
Velocity Models

V_P (km/s)	V_S (km/s)	Density (g/mL)	Thickness (km)	Q_P	Q_S
Sichuan					
4.8	2.7	2.2	6	200	100
6	3.4	2.4	4	600	300
6.2	3.5	2.6	15	600	300
6.6	3.8	2.8	15	600	300
8.08	4.47	3.37	—	800	400
Tibet					
6	3.4	2.4	10	600	300
6.2	3.5	2.6	15	600	300
5.9	3.1	2.6	20	600	300
6.6	3.8	2.8	10	600	300
8.08	4.47	3.37	—	800	400

Results

Geodetic Inversion

We consider the inversion of the geodetic data first because it consists of simple point measurements with no time dimension, which greatly simplifies the modeling and inversion. Thus, for this inversion alone we assume only one time interval of rupture for each subfault and no slip rate function. Figure 4 shows the resulting slip distribution on the fault. The calculated moment from this model is 1.03×10^{21} N · m. Figure 5 compares the data vectors of displacement with the predictions of the model. The uncertainties in the GPS observations, as given by Shen *et al.* (2009), lie in the range 2–5 mm for most stations regardless of the amplitude of the measurement. Therefore, the smaller, more distant observations have relatively larger uncertainties. Because we do not normalize the GPS measurements in the inversion, the smaller values with larger uncertainty have less weight. The solution in Figure 4 is remarkably similar to the results of other investigators (Shen *et al.*, 2009; de Michele *et al.*, 2010; Feng *et al.* 2010; Xu *et al.*, 2010) who have inverted either jointly or separately GPS and InSAR geodetic data. The main difference between these solutions is in the strength of a secondary source region on the Beichuan fault just southwest of the Gaochuan right bend (stepover in Fig. 3) and whether this source is mainly on the Beichuan or Pengguan faults. Our solution favors slip on the Pengguan fault.

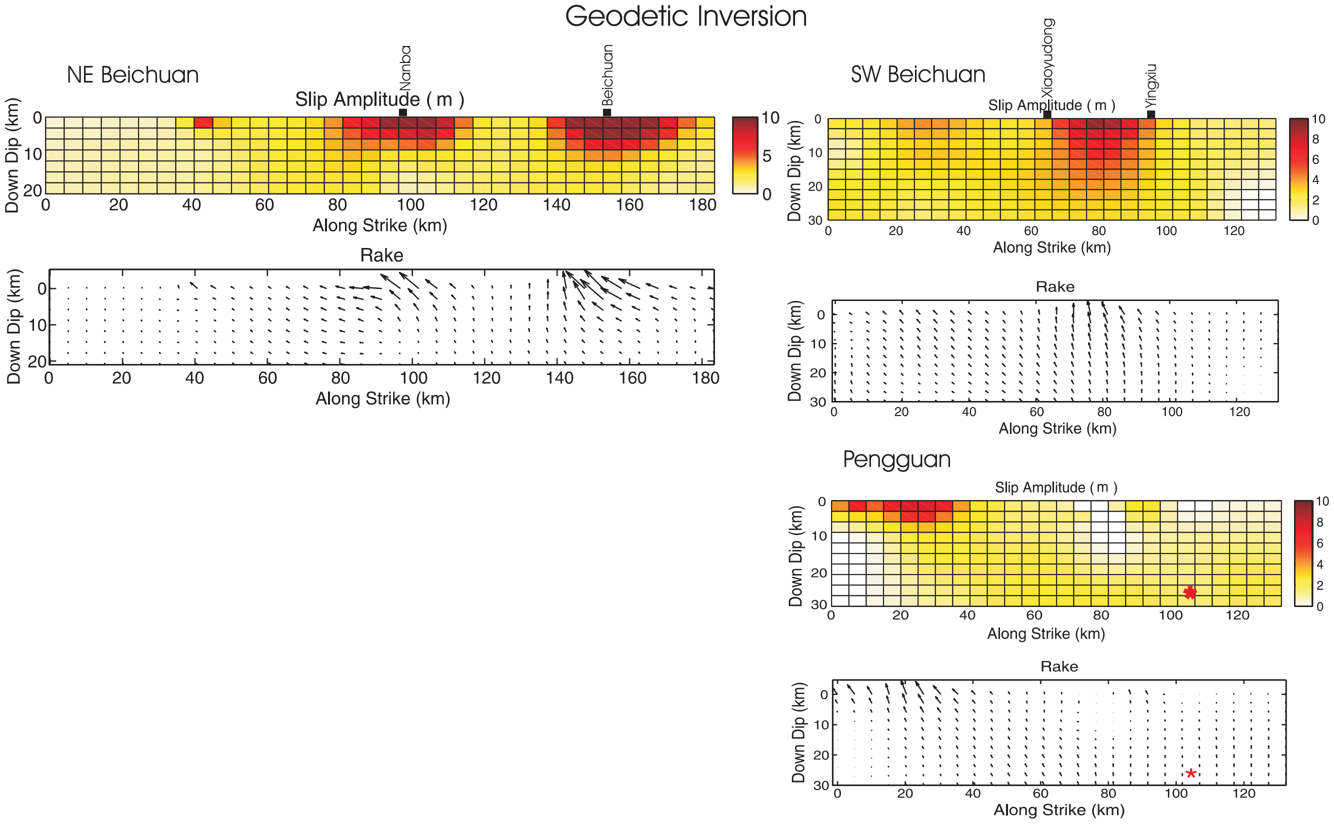

Figure 4. Slip distribution based on geodetic data.

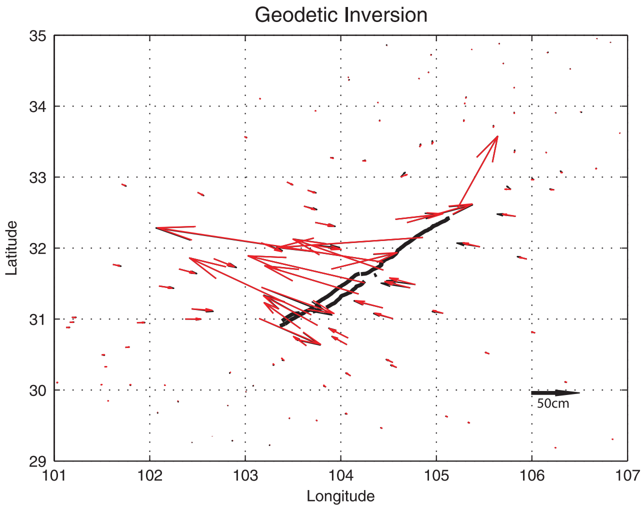

Figure 5. Comparison between observed surface horizontal deformation vectors (black) and predications of geodetic slip model (red) in Figure 4.

The geodetic inversion has a distinctive pattern of individual strong sources or asperities along the length of the rupture. These sources have been interpreted as resulting from the segmented nature of the fault system and the breaking of these barriers allowing the rupture to cascade through several fault segments resulting in a major M_w 7.9 earthquake (Shen *et al.*, 2009; Yu *et al.*, 2010).

Teleseismic Inversion

With the consideration of teleseismic waveforms, we develop a timing of rupture that is consistent with the geodetic observations. In other words, the model space of allowable teleseismic rupture models should encompass those with significant slip at the locations of the large slip patches in the geodetic model. For a simple fault with a single fault plane, this is generally a straightforward parameterization. With the multisegmented Wenchuan fault system, however, more consideration must be given to the possible rupture scenarios. The reported hypocenter (30.986°N, 103.364°E, U.S. Geological Survey; see Fig. 1) lies southwest of the town of Yingxiu at a depth of 12 km near the intersection of the low-angle Penguuan fault and high-angle Beichuan fault. The rupture could have initiated on the Pengguan fault or the Beichuan fault or ruptured both faults simultaneously. The teleseismic data alone are not capable of choosing between these different rupture models without additional constraints. To resolve this uncertainty, we first impose a reasonable upper bound on the rupture velocity. Given the shear-wave velocities of 3.4–3.5 km/s at seismogenic depths of our model and the observation that most earthquakes rupture at velocities near 0.8 V_S (Somerville *et al.*, 1999), we set the rupture velocity at 3.0 km/s. We will revisit the choice of 3.0 km/s and give more support for this value when we discuss our preferred rupture model based on the joint inversion of all three data sets. Rupture over 240 km, as in the Wenchuan earthquake, is not expected to maintain a constant velocity over its entire length. Our analysis suggests, however, that any large deviations in rupture velocity form an average value of 3.0 km/s, such as super-shear values, do not occur over a significant fraction of the fault plane. Our parameterization is linear and does not allow for a variable rupture velocity; the multitime interval model, however, does allow slip to occur later than the passage of the initial rupture front.

Given the location of the epicenter, allowing the rupture to initiate on the Beichuan fault or to rupture the Pengguan and Beichuan faults simultaneously would produce a nearly unilateral rupture to the northeast. The rupture scenario favored by the joint inversion of the complete data set begins on the Pengguan fault and proceeds northeast to the crosscutting Xiaoyudong fault, at which point rupture initiates on the Beichuan fault. Faulting then continues unilaterally on the Pengguan fault and bilaterally on the Beichuan fault. Because of the close proximity of these faults and the steep takeoff angles, the teleseismic data alone cannot distinguish between these scenarios, which yield nearly identical waveforms. Strong-motion stations near the southern end of the Beichuan fault rupture, however, discussed in the next section, clearly favor a section of fault rupturing to the southwest. We have not explored all possible rupture scenarios, such as reversed rupture direction on parts of one or more fault planes, but within the limitations of our parameterization, this is the simplest model that fits all three data sets. We note that Beroza and Spudich (1988) favor a model in which an asperity ruptured in the reverse direction, back toward the hypocenter, to explain the strong ground-motion records for the 1984 Morgan Hill, California, earthquake.

The slip distribution obtained from the inversion of the teleseismic data is shown in Figure 6. The estimated moment is 1.02×10^{21} $\mathrm{N \cdot m}$, nearly the same as obtained from the geodetic data. The geodetic data, however, show insensitivity to deeper slip (Ching *et al.*, 2007). In fact, one can see that the teleseismic solution puts considerably more deeper slip below 10 km on the Pengguan and northeast Beichuan segments. But, the teleseismic inversion, like the geodetic inversion, identifies several patches of elevated slip, although in different locations from the geodetic results. That there is more slip on the Pengguan segment in the teleseismic inversion is due to nearly equivalent timing observed at teleseismic distances for the Pengguan and Beichuan segments. Teleseismic data cannot distinguish between slip on the two closely spaced parallel faults. The differences between the geodetic and teleseismic results are resolved in the joint inversion discussed later. We also note that the joint inversion largely eliminates the edge effect of large slip along the bottom edge of the Pengguan and northeast Beichuan fault segments.

Figure 7 shows the comparison between the P-waveforms and the synthetics. Each waveform starts at the first arriving P wave from the hypocenter, picked from the unfiltered seismograms. The entire record is used in

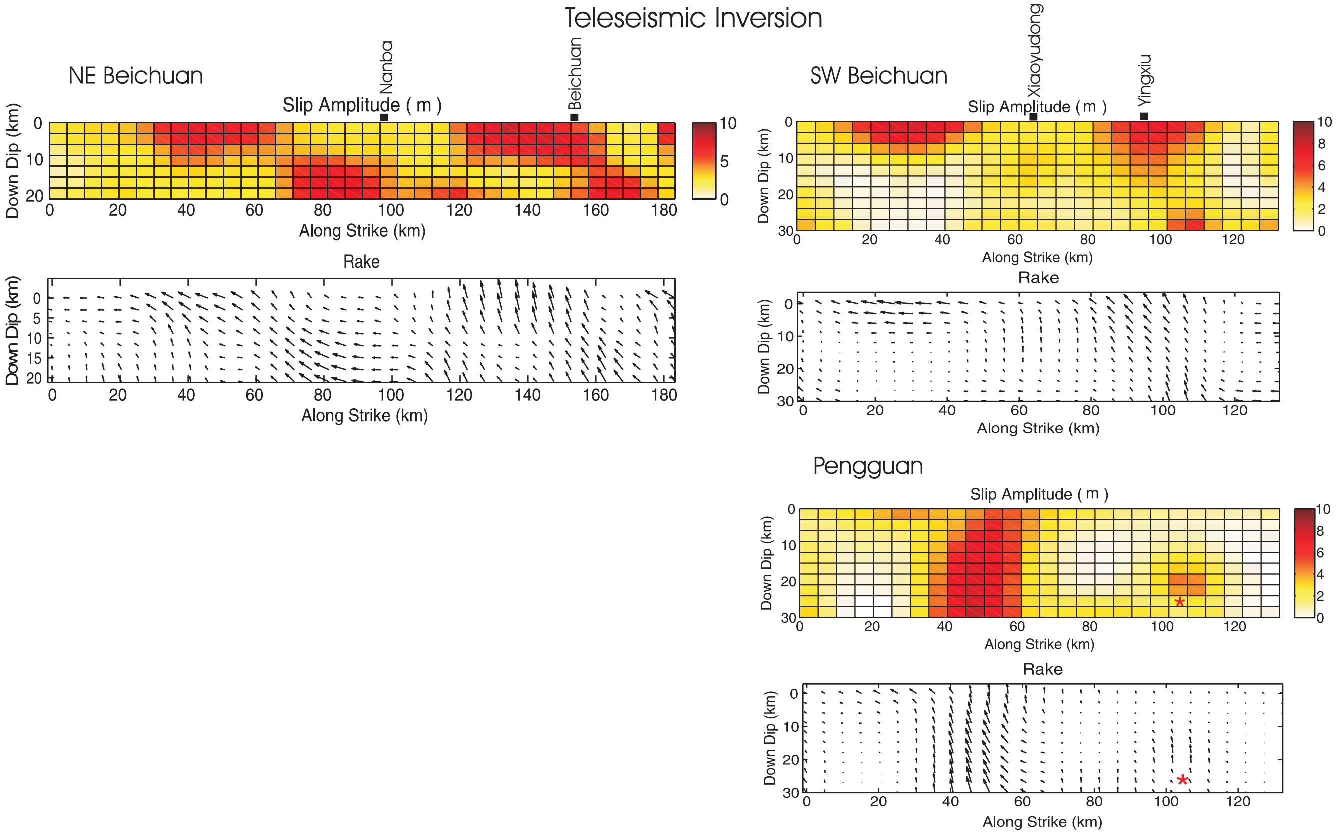

Figure 6. Slip distribution based on teleseismic data.

the inversion. Although this earthquake's location yields an advantageous azimuthal distribution of stations (Fig. 2), there are some closely spaced station pairs that may raise a question of bias. To investigate the stability of the results on the station distribution, we eliminated the stations LVZ, COLA, GNI, GRFO, and POHA and repeated the inversion. A nearly identical result was obtained, which was used to forward predict the omitted waveforms. Figure 7c shows the close match between the synthetic waveforms from the original inversion and the forward prediction.

Strong-Motion Inversion

As with the teleseismic data, the inversion process requires that the phase of interest arriving from the hypocenter be aligned with the corresponding phase in the data record. This alignment is straightforward for the teleseismic *P* waveforms. For strong-motion records, the preferred alignment phase is the *S* wave because it usually has the largest amplitude and is a major contributor to damage. The Wenchuan strong-motion records, however, are long and complex with arrivals from several subevents. To facilitate the alignment process, we started with acceleration and velocity records to emphasize the arrival times of individual phases. This alignment was then checked by forward modeling the strong-motion displacement records using the geodetic-derived slip model and our preferred rupture velocity of 3.0 km/s. Small time shifts were made as needed. The entire strong-motion record, including *P*-, *S*-, and surface-wave energy, is used in the inversion.

The preferred sequencing and direction of the fault ruptures could not be finalized until the joint inversion of the strong-motion data with the teleseismic and geodetic data. Just as with the teleseismic records by themselves, the strong-motion data alone cannot effectively distinguish between different rupture scenarios in the presence of complex fault planes and a large number of model parameters. By including the other data sets, the acceptable model space is restricted. Thus, the five time interval source parameterization fits the strong-motion data by itself remarkably well for both unilateral and bilateral rupture of the Beichuan fault. Figure 8 shows the fits to the data for our preferred model with bilateral rupture on the Beichuan fault from the Xiaoyudong fault. The estimated moment is 0.97×10^{21} N · m. The fit to the data is considerably better than one would expect given the geologic and topographic complexities of the Longmen Shan fault zone. This fit is made even more questionable when one considers the simplicity of our 1D velocity models. Our concerns are supported by the resulting slip distribution in Figure 9. The strong-motion slip model is very complex and has little or no resemblance to the geodetic and teleseismic inversions. We conclude that complexities in the propagation path are being mapped into the source model.

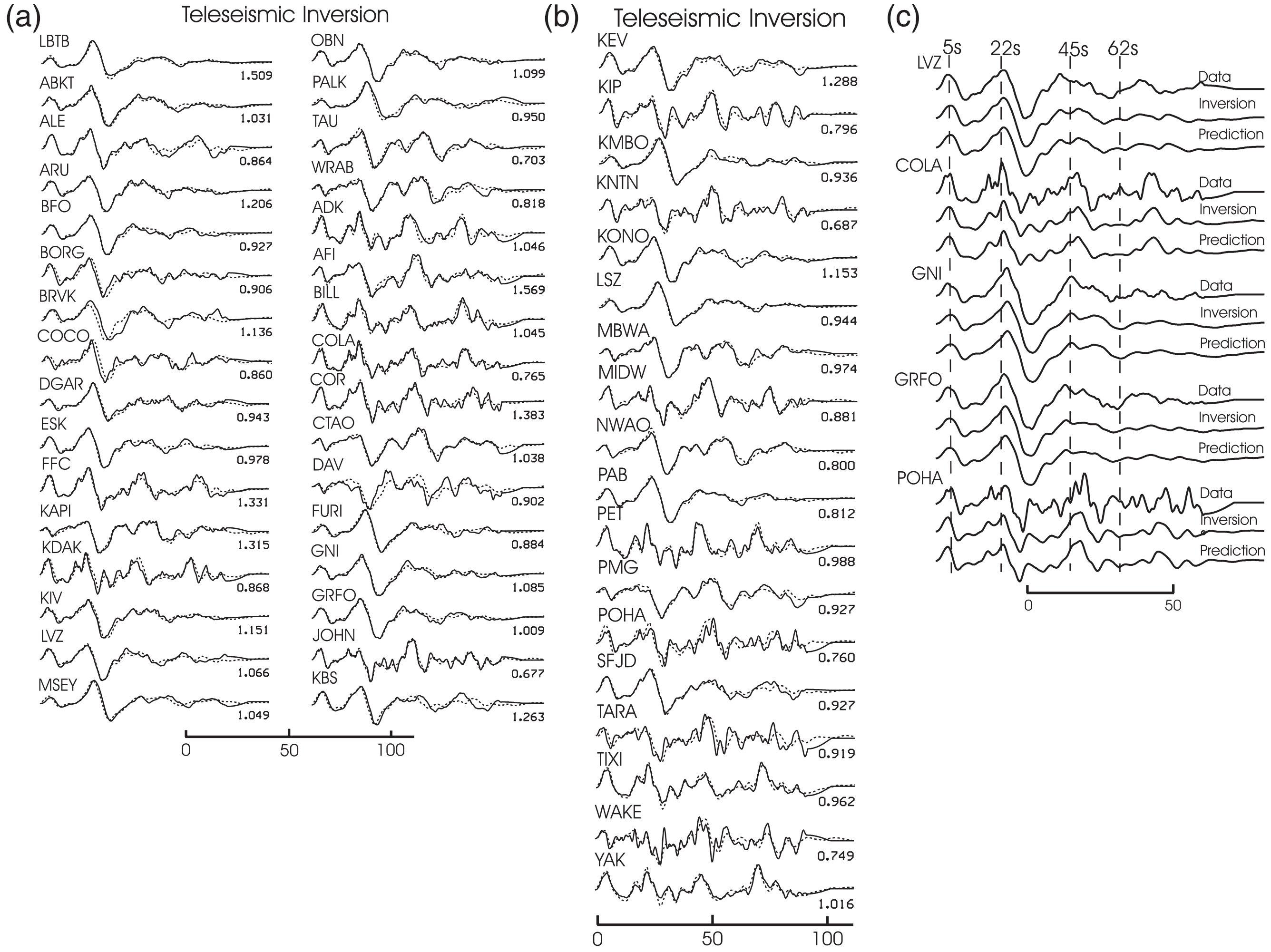

Figure 7. (a,b) Comparison between teleseismic broadband *P* waveforms bandpassed from 1 to 60 s (solid curves) and predictions of teleseismic slip model (dashed curves) in Figure 6. Number to right is the ratio of the peak synthetic amplitude to the peak data amplitude. Time scale in seconds. (c) Stability test results of the teleseismic inversion by removing the closely paired stations: LVZ, COLA, GNI, GRFO, and POHA. The inversion synthetic uses all of the stations in the inversion. The prediction synthetic is predicted from the source model obtained from omitting the five stations. All curves are plotted on the same scale for a given station. The four times (5, 22, 45, and 62 s) correlate with the rupturing of major slip patches in the joint inversion (Fig. 11). Time scale in seconds.

This pitfall can easily occur and lead to incorrect conclusions with any source inversion using only strong-motion data where the Green's functions do not adequately represent the true propagation path effects. An interesting counter example is the data set for the 2004 Parkfield, California, earthquake. For this event, there are 54 strong-motion records over a 50-km-long section of fault (Hartzell *et al.*, 2007). Contrast this distribution with that of the Wenchuan earthquake with 40 stations over a distance of 400 km. Even though there are still questions about the slip distribution for the Parkfield earthquake, the strong-motion data alone in this case are able to do a better job of resolving the slip because of its finer spatial sampling.

Stations near the southwestern end of the Beichuan fault rupture are particularly diagnostic in choosing between different rupture models in the joint inversion of the three data sets. The southern stations show two main packets of energy separated by about 25 s (Fig. 10). The first comes from early rupture on the Pengguan fault. The second comes from slip on the Beichuan fault. If the rupture is allowed to proceed unilaterally to the northeast on the Beichuan fault, the second pulse is washed out at these stations because they lie at a back azimuth from the source. This problem is overcome by a bilateral rupture on the Beichuan fault from the point of intersection with the cross-cutting Xiaoyudong fault. The fits in Figure 10 are not as good as those in Figure 8 because the solution is required to be consistent with the geodetic and teleseismic data sets and the inversion is not allowed to over fit phase and amplitude information in the strong-motion waveforms with imprecise Green's functions. The fits, however, are adequate to conclude that there is rupture to the southwest over a section of the Beichuan fault because of the prominence of the phase produced in the strong-motion records.

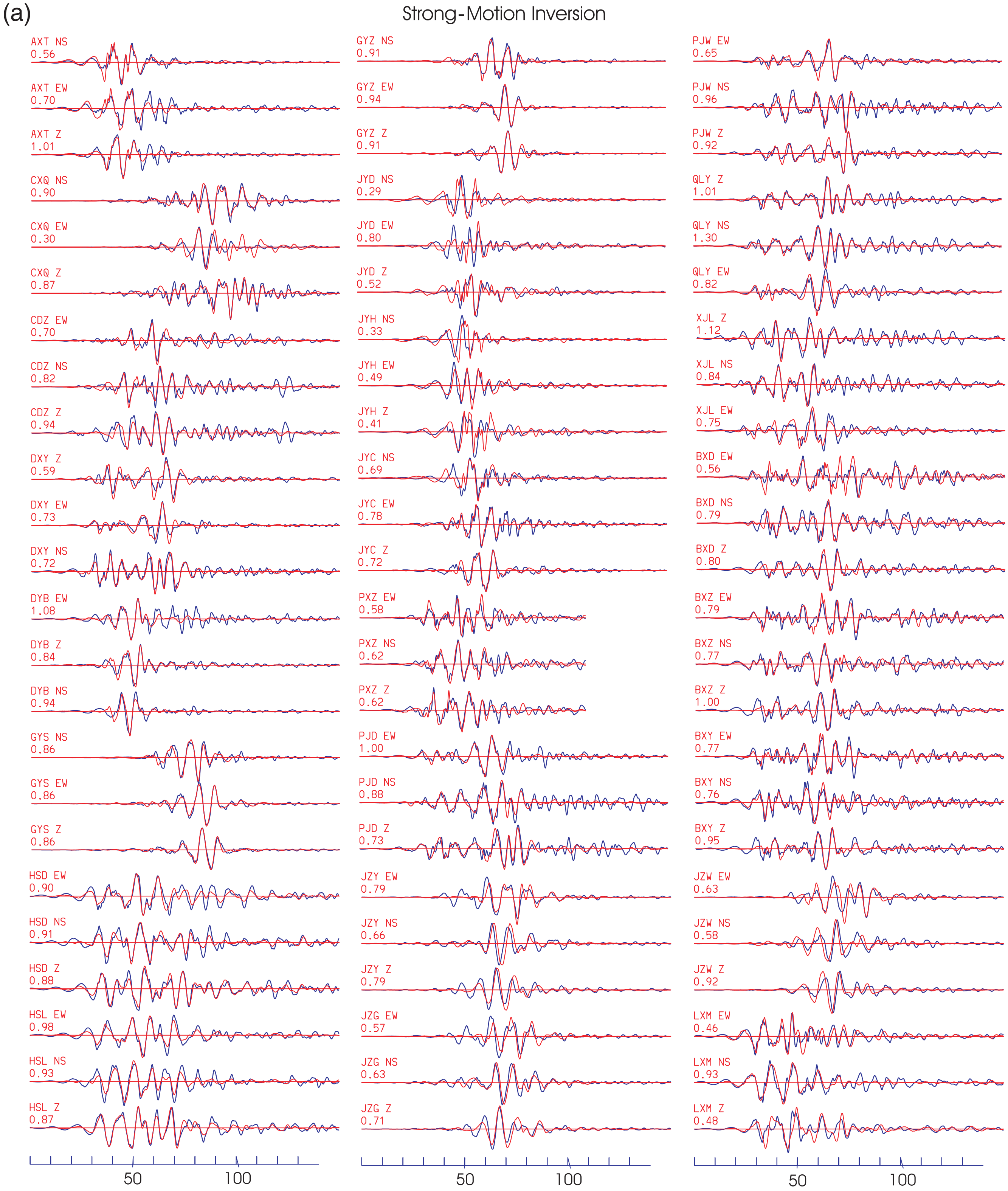

Figure 8. (a,b) Comparison between strong-motion displacement records bandpassed from 1 to 12.5 s (bold blue curves) and predictions of strong-motion slip model (thin red curves) in Figure 9. Number below station code is the ratio of the peak synthetic amplitude to the peak data amplitude. Time scale in seconds. (*Continued*)

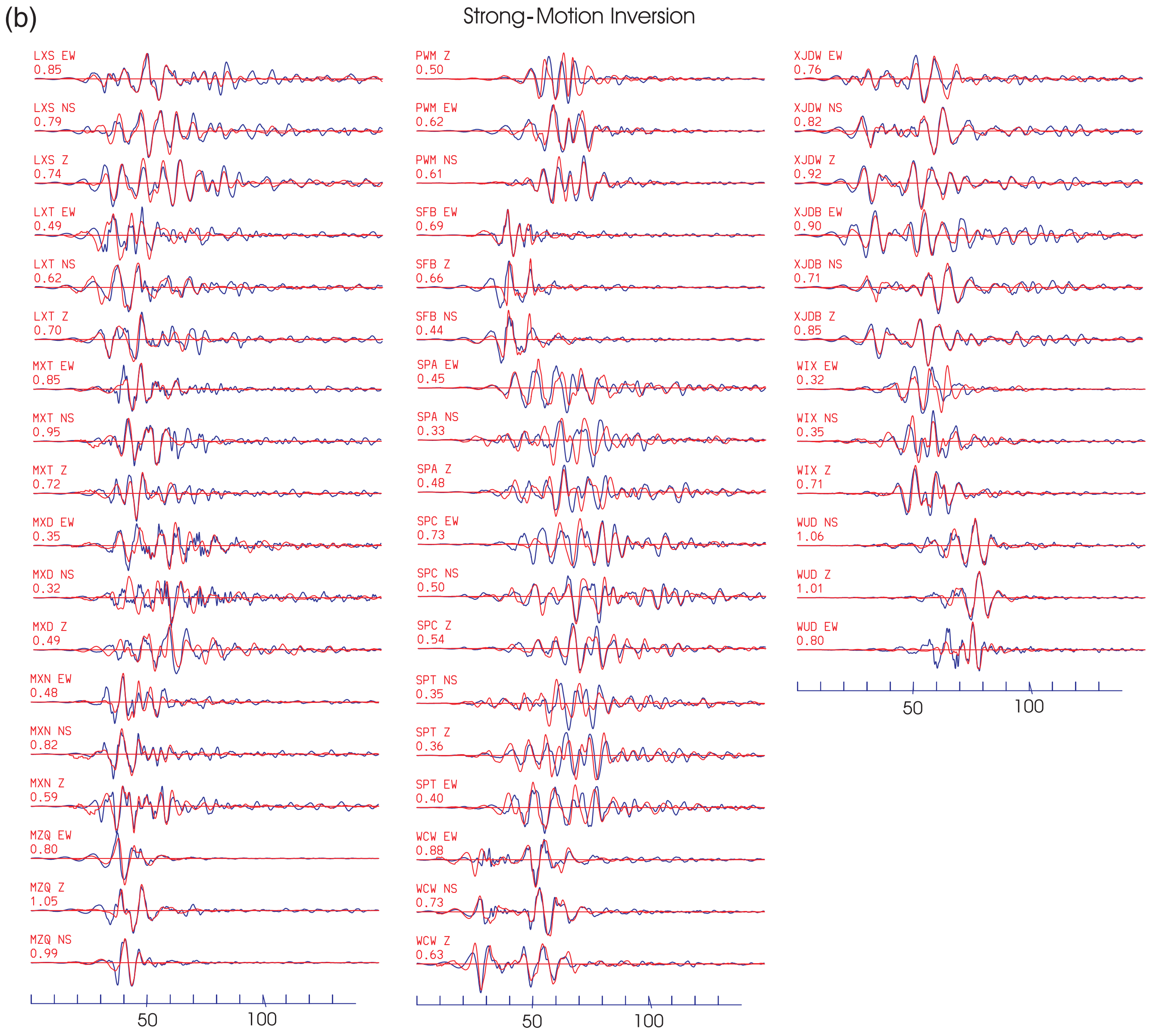

Figure 8. Continued.

Joint Inversion

With a joint inversion, the question arises of how to weight the different data sets. Kaverina *et al.* (2002) have suggested weighting different data sets by the ratio of the independently determined smoothing parameters for each data set. Hernandez *et al.* (1999) introduce a relative weighting factor obtained from the covariance matrix of the data. Hernandez *et al.* (1999), later expanded on by Custodio *et al.* (2009), used a two-step inversion where the temporal model parameters (rise time, rupture velocity, etc.) are inverted using seismic data and the slip distribution constrained by the results of the geodetic inversion. We invert the geodetic and seismic data simultaneously with a weighting procedure similar to Kaverina *et al.* (2002), Hernandez *et al.* (1999), and Wald and Graves (2001). We calculate the sum of the absolute values of the elements of the synthetics matrix, **A**, associated with each data set. The relative weights are then calculated by taking the ratio of the sums between the different data sets such that each data set has an equal amplitude contribution in the **A** matrix. After the weights are applied to the elements of the **A** matrix, the smoothing and minimization constraint weights are then calculated as before. This procedure assures that the different data sets have the same overall contribution to the solution.

The slip distribution for the joint inversion is shown in Figure 11. The moment is 1.04×10^{21} N · m. The solution honors the locations of the major slip patches found from the geodetic inversion, but the slip distribution with depth is augmented based on the influence of the teleseismic data.

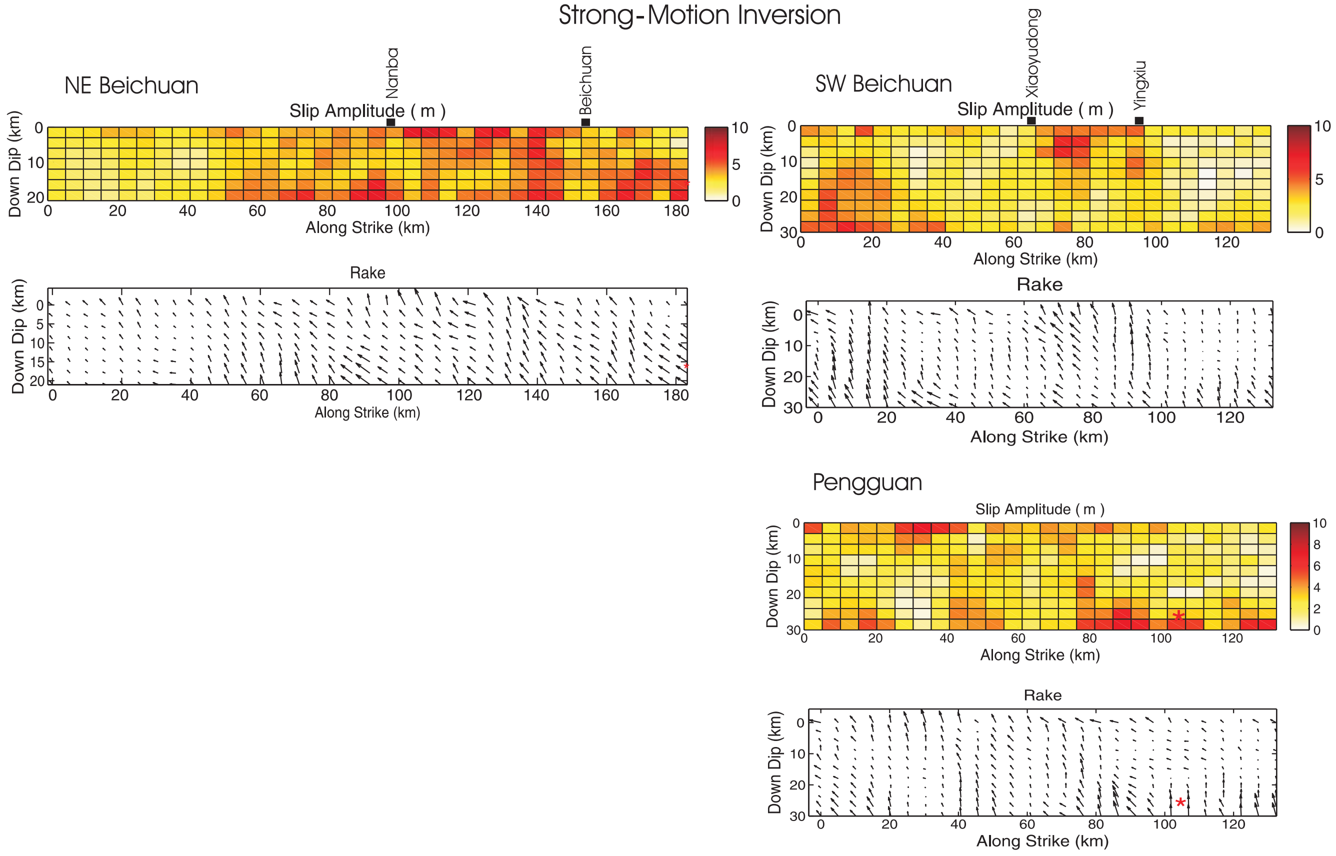

Figure 9. Slip distribution based on strong-motion data.

The slip distribution with depth is largely defined within the limits of the parameterized Pengguan and northeast Beichuan fault segments. Slip on the southwest Beichuan fault is still large at the bottom edge of the fault at a depth of 21 km. We conclude that deeper slip may have occurred in this region. Twenty kilometers, however, is the depth at which the Beichuan fault is hypothesized to transition into a near horizontal detachment zone (Hubbard *et al.*, 2010), and the specifics of a fault parameterization at these depths would be based largely on conjecture. Therefore, we have not attempted to model deeper slip. There is enough flexibility in the multitime-interval parameterization to allow the teleseismically determined slip patches to move to the locations of the geodetically determined slip. Note that the teleseismic part of the solution is the one that is modified rather than the geodetic because the geodetic slip patches cannot be moved and still fit the data. The teleseismic records are insensitive to where the slip occurs as long as the timing of the slip is consistent with the waveforms.

Three large patches of slip are apparent along the Beichuan fault: between the cities of Yingxiu and Xiaoyudong and near the cities of Beichuan and Nanba. These high-slip patches correspond with large observed surface offsets of approximately 6.2-m vertical and 4.5-m horizontal between Yingxiu and Xiaoyudong, 6.5-m vertical and 4.3-m horizontal near Beichuan, and 2.5-m vertical and 3.0-m horizontal near Nanba (Yu *et al.*, 2010). The locations of these slip concentrations also agrees with the results of Shen *et al.* (2009) from the inversion of GPS and InSAR data and is the probable explanation why the cities of Yingxiu, Beichuan, and Nanba experienced the greatest damage along the fault zone (Shen *et al.*, 2009). We can now offer additional support for our rupture velocity of 3.0 km/s. Figure 11 shows the location of the rupture front at four times after the initiation of rupture (5, 22, 45, and 62 s) as related to major slip zones. Also indicated by the dashed lines is the spatial extent of the fault plane involved in rupture at the four times. Each of these zones defined by the dashed lines is 30-km wide dictated by the rupture velocity of 3.0 km/s and the total allowed rise time of 10 s. These four times are also indicated in Figure 7c relative to significant arrivals in the teleseismic data and synthetic waveforms. We deduce from these plots that a rupture velocity significantly different from 3 km/s would not yield agreement in the joint inversion between the major source locations from the geodetic inversion, prominent arrivals in the teleseismic waveforms, the observed large surface offsets, and the locations of heavily damaged cities.

The model fit to the different data sets is shown in Figure 12. Both the geodetic and teleseismic data are fit nearly as well as in the individual inversions. The fit to the strong-motion data, however, shows degradation over the fit of the strong-motion inversion (L2 norms joint inversion:

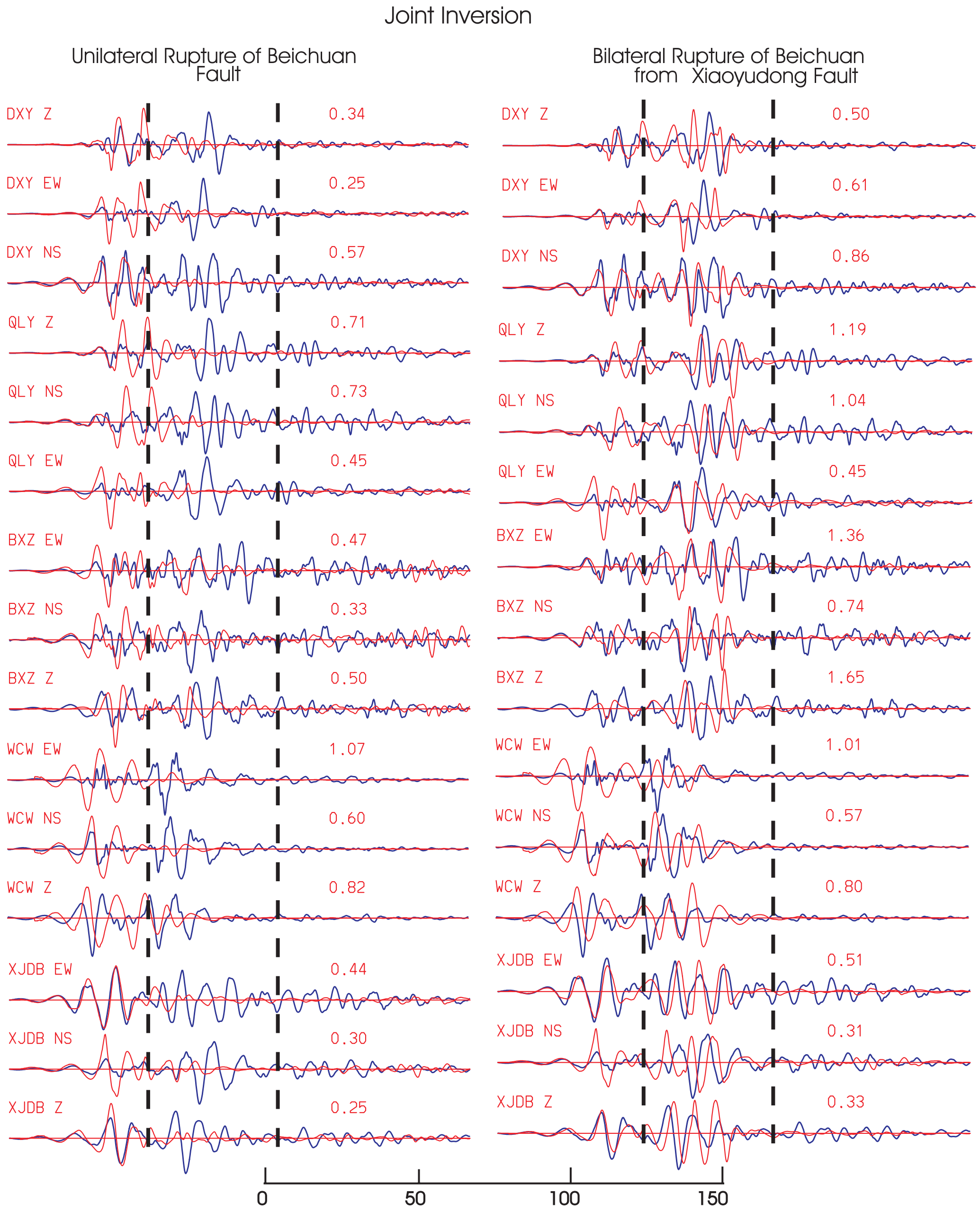

Figure 10. Comparison of two rupture scenarios for the Wenchuan earthquake considering unilateral and bilateral rupture of the Beichuan fault and using all three data sets: geodetic, teleseismic, and strong motion. Vertical dashed lines bracket second arrival seen on stations at the southwestern end of the Beichuan fault. Time scale in seconds.

strong motion = 76.6, teleseismic = 29.6, geodetic = 17.8; L2 norms individual inversions: strong motion = 42.8, teleseismic = 23.0, geodetic = 17.6). This degradation is expected given our simplistic 1D velocity models and the reduced complexity of the slip distribution in the joint inversion.

Discussion and Conclusions

The inversions of the individual data sets and the joint inversion of the geodetic, teleseismic, and strong-motion data show that a distorted view of the slip distribution can be obtained from any one data set by itself. The geodetic data gives a good picture of the locations of major shallow slip patches (< 10-km depth) along the Pengguan and Beichuan faults and yields a scenario of cascading asperities or breaking barriers that carries the rupture forward. The geodetic data, however, are not sensitive to deeper slip. Teleseismic records are useful for defining the deeper slip but are insensitive to the exact location of this slip with multiple fault planes. Fitting of teleseismic records is driven by timing, not location. In a joint inversion with geodetic data, the slip is moved to agree with the geodetically determined slip, as

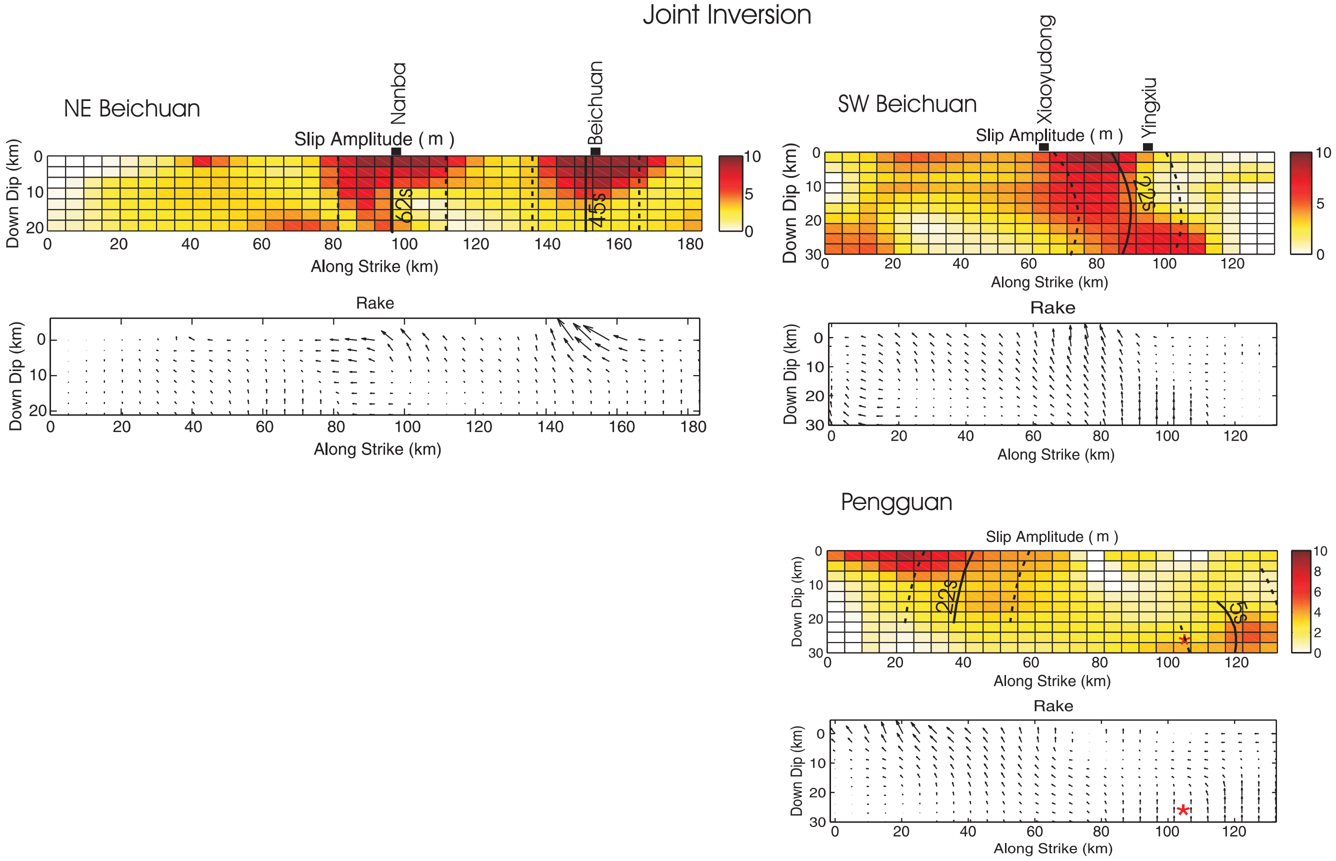

Figure 11. Slip distribution based on joint inversion of geodetic, teleseismic, and strong-motion data. Rupture front is shown at the four times 5, 22, 45, and 62 s after the initiation of rupture. Area of the fault plane allowed to slip at each time for a rise time of 10 s, dashed lines. These times correlate with major slip patches and also with prominent arrivals in the teleseismic P waveforms (Fig. 7c).

the geodetic data cannot tolerate a change in the position. The strong-motion data proved to be useful for determining the sequencing of the rupturing of the different fault segments from directivity arguments. Without the near-field directivity information contained in the strong-motion records in conjunction with the other data sets, it would be difficult to distinguish between unilateral and bilateral rupture on the Beichuan fault.

Analysis of the Wenchuan earthquake points out the strengths and weaknesses of the different data sets. Geodetic data are clearly useful for unraveling the spatial complexities of a complex rupture sequence because the time element is removed from the problem. Near-field strong-motion records could be useful for this purpose; most regions, however, do not have sufficient station coverage, and calculating accurate Green's functions can be problematic. On the other hand, geodetic measurements say nothing about the evolution of the rupture, which can only be obtained from waveform data. Thus, detailed imaging of complex ruptures on multiple fault planes requires data that encompass both as large a bandwidth as can be accurately modeled and as large a sampling of takeoff angle as available. Teleseismic data are insensitive to lateral variations in position of slip on a fault because of the steep takeoff angle with slip position governed mainly by timing. Strong-motion data have a greater resolution of position by its moderate takeoff angles and strong directivity effects. Strong-motion data, however, are more difficult to model with certainty because of often inadequate Green's functions and spatial under sampling. Similar conclusions concerning the value of multiple data sets have been reached by Delouis *et al.* (2002) and other studies.

The Wenchuan earthquake has rupture characteristics similar to two recent intraplate events of similar magnitude: the 2001 M_w 7.8 Kunlun, Tibet, and the 2002 M_w 7.9 Denali, Alaska, earthquakes. All three of these events are predominantly unilateral ruptures with slip distributions characterized by major slip patches or asperities (Lin *et al.*, 2003; Frankel, 2004; Ozacar and Beck, 2004). In addition, each has its peak slip far removed from the hypocenter. In the case of the Denali earthquake, Oglesby *et al.* (2004) conclude that stress heterogeneity in the tectonic stress field must be invoked to explain the heterogeneous slip pattern. The peak slip of 10 m for the Wenchuan earthquake is consistent with the Denali earthquake, where estimates range from 9 m (Ozacar and Beck, 2004) to 13.4 m (Liao and Huang, 2008). Estimates of average rupture velocity are similar or somewhat higher for the Denali earthquake, with values of 2.95 km/s (Liao and Huang, 2008) and 3.2 km/s (Ozacar

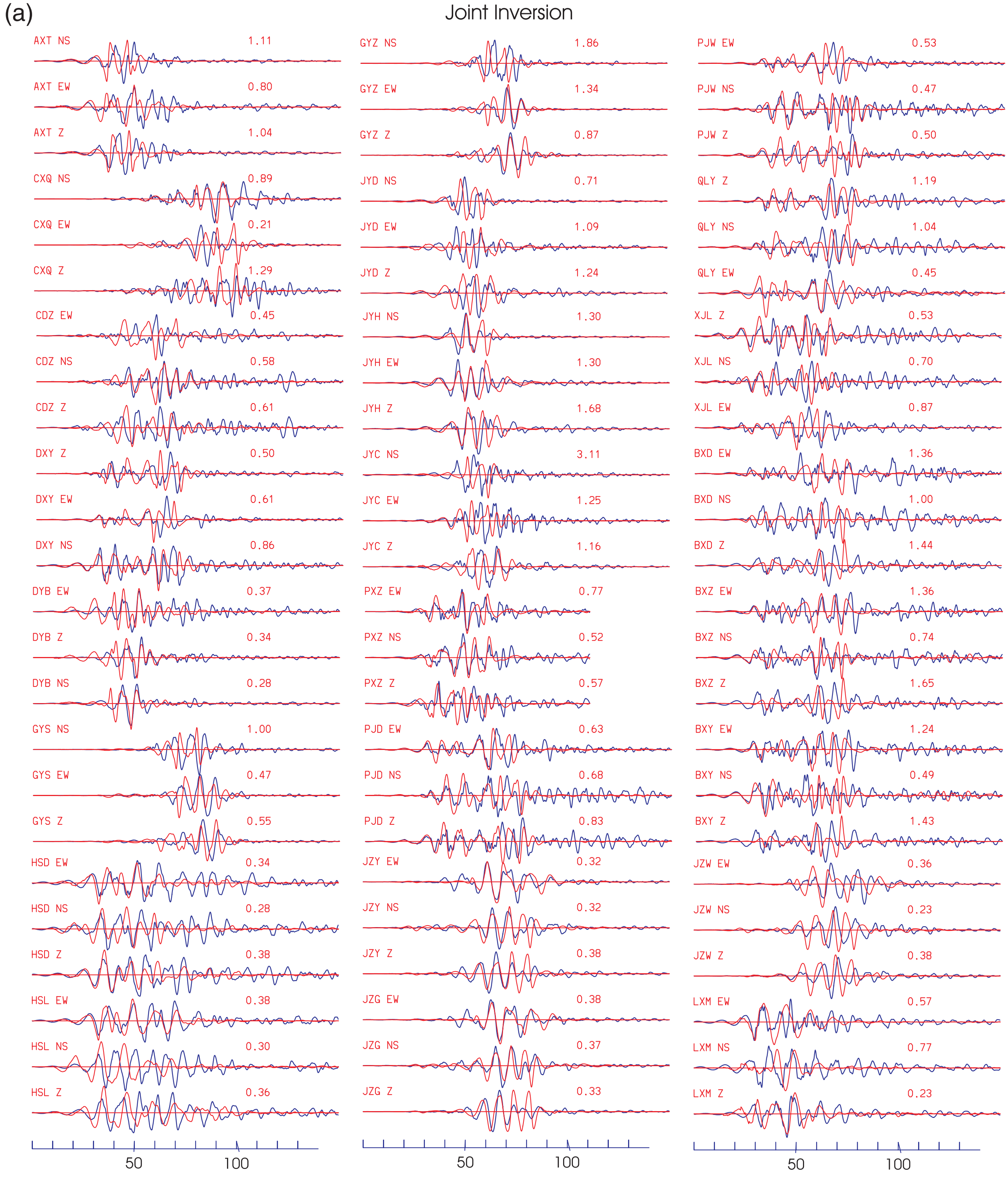

Figure 12. (a–d) Comparison of data and synthetics for joint inversion slip model in Figure 11. Number to right is the ratio of the peak synthetic amplitude to the peak data amplitude. Time scale in seconds. (*Continued*)

and Beck, 2004). A rupture velocity near the shear-wave velocity of 3.4 km/s is reported for the Kunlun earthquake, however (Lin *et al.*, 2003; Ozacar and Beck, 2004).

Our source model, in which the rupture jumps from the Pengguan fault to the Beichuan fault along the cross-cutting Xiaoyudong fault, points out the importance of this short-tear

Figure 12. Continued.

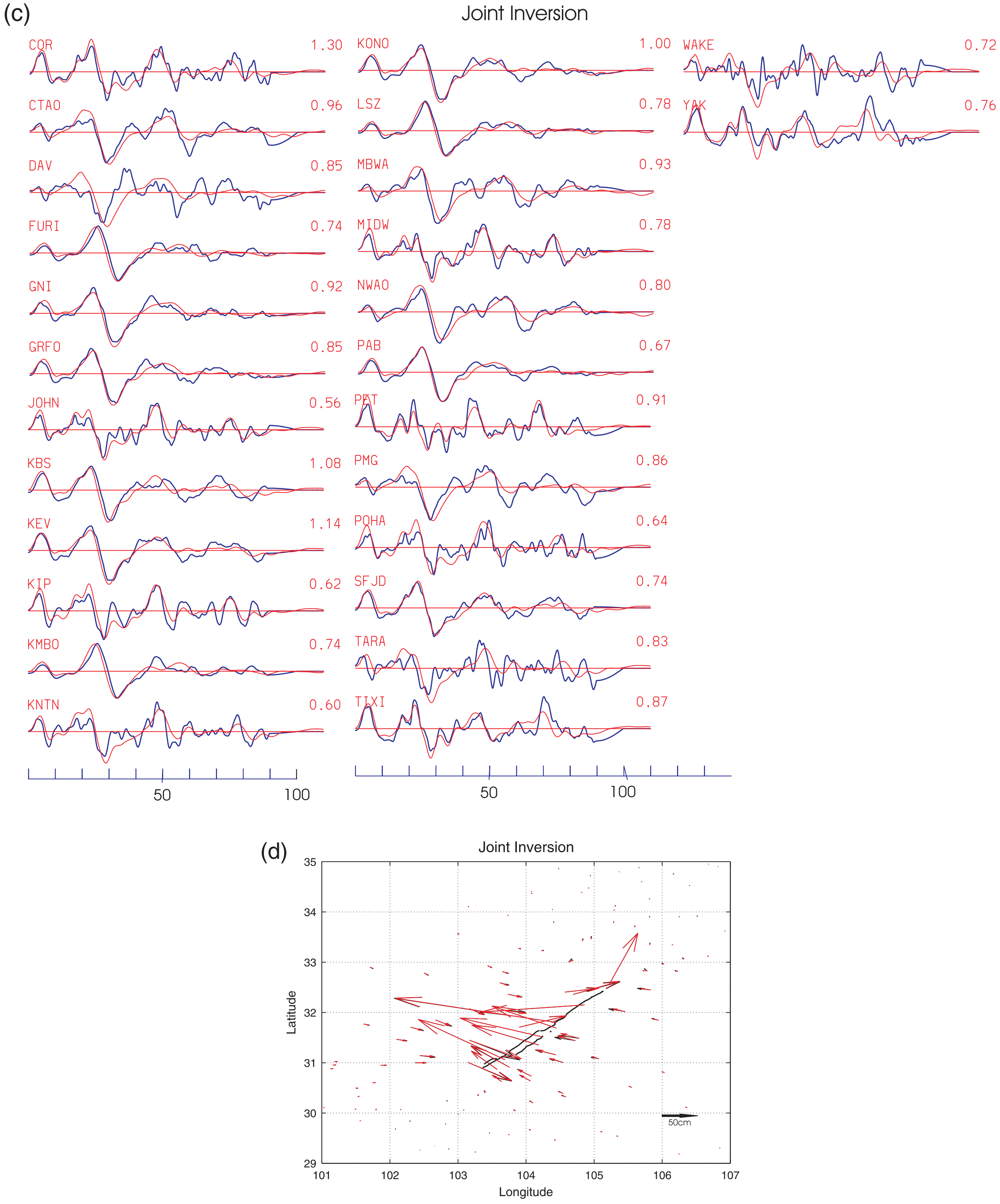

Figure 12. Continued.

fault in the evolution of the Wenchuan earthquake. This rupture scenario also raises the interesting question: Without the Xiaoyudong fault, would the Wenchuan earthquake have stayed on the Pengguan fault and been a much smaller and less destructive event?

Data and Resources

The geodetic data were provided by Zheng-Kang Shen of the State Key Laboratory of Earthquake Dynamics, Institute of Geology, China Earthquake Administration, Beijing, China (Shen *et al.*, 2009). The teleseismic records are available from the IRIS Data Management Center, http://www.iris.edu/data/ (last accessed August 2011). The strong-motion records were obtained through a cooperative agreement between the Institute of Engineering Mechanics, China Earthquake Administration, Harbin, China, and the U.S. Geological Survey. We reference teleseismic slip models by Ji and Hayes, 2008, http://earthquake.usgs.gov/earthquakes/eqinthenews/2008/us2008ryan/finite_fault.php (last accessed January 2011), and Nishimura and Yagi, 2008, http://www.geol.tsukuba.ac.jp/~nisimura/20080512 (last accessed January 2011).

Acknowledgments

The authors are grateful to Zheng-Kang Shen for providing the geodetic data. The strong-motion data were generously provided by the Institute of Engineering Mechanics, China Earthquake Administration, Harbin, China, director Wen Ruizhi (current director Sun Bai-Tao). The authors thank Chen Ji for his local velocity model. Richard Dart assisted with the Geographic information system (GIS) figures. The manuscript was improved by comments from Arthur Frankel, Martin Mai, and an anonymous reviewer. The work was completed while one of the authors (C.M.) was on a sabbatical leave sponsored by the Direccion General de Asuntos del Personal Academico (DGAPA).

References

Beroza, G. C., and P. Spudich (1988). Linearized inversion for fault rupture behavior; application to the 1984 Morgan Hill, California, earthquake, *J. Geophys. Res.* **93,** 6275–6296.

Bjerrum, L. W., M. B. Sorensen, and K. Atakan (2010). Strong ground-motion simulation of the 12 May 2008 M_w 7.9 Wenchuan earthquake, using various slip models, *Bull. Seismol. Soc. Am.* **100,** 2396–2424.

Chavez, M., E. Cabrera, R. Madariaga, H. Chen, N. Perea, D. Emerson, A. Salazar, M. Ashworth, Ch. Moulinec, X. Li, M. Wu, and G. Zhao (2010). Low-frequency 3D wave propagation modeling of the 12 May 2008 M_w 7.9 Wenchuan earthquake, *Bull. Seismol. Soc. Am.* **100,** 2561–2573.

Ching, K.-E., R.-J. Rau, and Y. Zeng (2007). Coseismic source model of the 2003 M_w 6.8 Chengkung earthquake, Taiwan, determined from GPS measurements, *J. Geophys. Res.* **112,** 31 pp., B06422, doi: 10.1029/2006JB004439.

Custodio, S., M. T. Page, and R. J. Archuleta (2009). Constraining earthquake source inversions with GPS data: 2. A two-step approach to combine seismic and geodetic data sets, *J. Geophys. Res.* **114,** 20 pp., B01315, doi: 10.1029/2008JB005746.

Dai, F. C., C. Xu, X. Yao, L. Xu, X. B. Tu, and Q. M. Gong (2011). Spatial distribution of landslides triggered by the 2008 M_S 8.0 Wenchuan earthquake, China, *J. Asian Earth Sci.* **40,** 883–895.

de Michele, M., D. Raucoules, J. de Sigoyer, M. Pubellier, and N. Chamot-Rooke (2010). Three-dimensional surface displacement of the 2008 May 12 Sichuan earthquake (China) derived from synthetic aperture radar: Evidence for rupture on a blind thrust, *Geophy. J. Inter.* **183,** 1097–1103.

Delouis, B., D. Giardini, P. Lundgren, and J. Salichon (2002). Joint inversion of InSAR, GPS, teleseismic, and strong-motion data for the spatial and temporal distribution of earthquake slip: Application to the 1999 Izmit mainshock, *Bull. Seismol. Soc. Am.* **92,** 278–299.

Densmore, A. L., Y. Li, N. J. Richardson, R. Zhou, M. Ellis, and Y. Zhang (2010). The role of late Quaternary upper-crustal faults in the 12 May 2008 Wenchuan earthquake, *Bull. Seismol. Soc. Am.* **100,** 2700–2712.

Feng, G.-C., E. A. Hetland, X.-L. Ding, Z.-W. Li, and L. Zhang (2010). Coseismic fault slip of the 2008 M_w 7.9 Wenchuan earthquake estimated from InSAR and GPS measurements, *Geophys. Res. Lett.* **37,** L01302.

Frankel, A. (2004). Rupture process of the M 7.9 Denali fault, Alaska, earthquake: Subevents, directivity, and scaling of high-frequency ground motions, *Bull. Seismol. Soc. Am.* **94,** S234–S255.

Furuya, M., T. Kobayashi, Y. Takada, and M. Murakami (2010). Fault source modeling of the 2008 Wenchuan earthquake based on ALOS/PALSAR data, *Bull. Seismol. Soc. Am.* **100,** 2750–2766.

Gardner, M. A., L. Ramirez-Guzman, S. Hartzell, and W. D. Mooney (2011). A 3D crustal velocity model of the Longmen Shan fault zone in Sichuan, China (abstract), Geological Society of America, Minneapolis, Minnesota, October 9–12, 2011.

Ghasemi, H., Y. Fukushima, K. Koketsu, H. Miyake, Z. Wang, and J. G. Anderson (2010). Ground-motion simulation for the 2008 Wenchuan, China, earthquake using the stochastic finite-fault method, *Bull. Seismol. Soc. Am.* **100,** 2476–2490.

Hansen, P. C. (1998). *Rank-deficient and discrete ill-posed problems, numerical aspects of linear inversion*, Society for Industrial and Applied Mathematics, Philadelphia.

Hartzell, S., P.-C. Liu, C. Mendoza, C. Ji, and K. M. Larson (2007). Stability and uncertainty of finite-fault slip inversions: Application to the 2004 Parkfield, California, earthquake, *Bull. Seismol. Soc. Am.* **97,** 1911–1934.

Hartzell, S. H., and T. H. Heaton (1983). Inversion of strong ground motion and teleseismic waveform data for the fault rupture history of the 1979 Imperial Valley, California, earthquake, *Bull. Seismol. Soc. Am.* **73,** 1553–1583.

Helmberger, D. V. (1983). Theory and application of synthetic seismograms, in *Earthquakes: Observations, Theory, and Interpretation*, H. Kanamori and E. Boschi (Editors), North-Holland Publishing Company, Amsterdam, 174–222.

Hernandez, B., F. Cotton, and M. Campillo (1999). Contribution of radar interferometry to a two-step inversion of the kinematic process of the 1992 Landers earthquake, *J. Geophys. Res.* **104,** 13,083–13,099.

Hubbard, J., J. H. Shaw, and Y. Klinger (2010). Structural setting of the 2008 M_w 7.9 Wenchuan, China, earthquake, *Bull. Seismol. Soc. Am.* **100,** 2713–2735.

Kaverina, A., D. Dreger, and E. Price (2002). The combined inversion of seismic and geodetic data for the source process of the 16 October 1999 M_w 7.1 Hector Mine, California, earthquake, *Bull. Seismol. Soc. Am.* **92,** 1266–1280.

Kurahashi, S., and K. Irikura (2010). Characterized source model for simulating strong ground motions during the 2008 Wenchuan earthquake, *Bull. Seismol. Soc. Am.* **100,** 2450–2475.

Lawson, C. L., and R. J. Hanson (1974). *Solving Least Squares Problems*, Prentice-Hall, Inc., Englewood Cliffs, New Jersey, 340 pp.

Li, H., W. Su, C.-Y. Wang, Z. Huany, and Z. Lv (2010). Ambient noise Love wave tomography in the eastern margin of the Tibetan plateau, *Tectonophysics* **491,** 194–204.

Liao, B.-Y., and H.-C. Huang (2008). Rupture process of the 2002 M_w 7.9 Denali earthquake, Alaska, using a newly devised hybrid blind deconvolution method, *Bull. Seismol. Soc. Am.* **98,** 162–179.

Lin, A., M. Kikuchi, and B. Fu (2003). Rupture segmentation and process of the 2001 M_w 7.8 central Kunlun, China, earthquake, *Bull. Seismol. Soc. Am.* **93,** 2477–2492.

Liu-Zeng, J., L. Wen, J. Sun, Z. Zhang, G. Hu, X. Xing, L. Zeng, and Q. Xu (2010). Surficial slip and rupture geometry on the Beichuan fault near Hongkou during the M_w 7.9 Wenchuan earthquake, China, *Bull. Seismol. Soc. Am.* **100,** 2615–2650.

Mendoza, C., and S. Hartzell (2012). Finite-fault source inversion using teleseismic *P* waves: Simple parameterization and rapid analysis, *Bull. Seismol. Soc. Am.* (in press).

Oglesby, D. D., D. S. Dreger, R. A. Harris, N. Ratchkovski, and R. Hansen (2004). Inverse kinematic and forward dynamic models of the 2002 Denali fault earthquake, Alaska, *Bull. Seismol. Soc. Am.* **94,** S214–S233.

Ozacar, A. A., and S. L. Beck (2004). The 2002 Denali fault and 2001 Kunlun fault earthquakes: Complex rupture processes of two large strike-slip events, *Bull. Seismol. Soc. Am.* **94,** S278–S292.

Shao, G., C. Ji, Z. Lu, K. Hudnut, J. Liu, W. Zhang, and Q. Wang (2010). Slip history of the 2008 M_w 7.9 Wenchuan earthquake constrained by jointly inverting seismic and geodetic observations (abstract S52B-04), *AGU*, San Francisco, California, 13–17 December 2010, (Fall Meet.), S52B-04.

Shen, Z.-K., J. Sun, P. Zhang, Y. Wan, M. Wang, R. Burgmann, Y. Zeng, W. Gan, H. Liao, and Q. Wang (2009). Slip maxima at fault junctions and rupturing of barriers during the 2008 Wenchuan earthquake, *Nat. Geosci.* **2,** 718–724.

Somerville, P., K. Irikura, R. Graves, S. Sawada, D. Wald, N. Abrahamson, Y. Iwasaki, T. Kagawa, N. Smith, and A. Kowada (1999). Characterizing crustal earthquake slip models for the prediction of strong ground motion, *Seismol. Res. Lett.* **70,** 59–80.

Wald, D. J., and R. W. Graves (2001). Resolution analysis of finite fault source inversion using one- and three-dimensional Green's functions, II. Combined seismic and geodetic data, *J. Geophys. Res.* **106,** 8767–8788.

Wei, Z., S. Yang, and C. XiaoFei (2008). Numerical simulation of strong ground motion for the M_S 8.0 Wenchuan earthquake of 12 May 2008, *Sci. China Ser. D: Earth Sci.* **51,** 1673–1682.

Working Group of the Crustal Motion Observation Network of China Project (WGCMONCP) (2008). Coseismic displacement field of the 2008 M_S 8.0 Wenchuan earthquake determined by GPS, *Sci. China Ser. D* **38,** 1195–1206 (in Chinese).

Xie, X., and Z. X. Yao (1989). A generalized reflection-transmission coefficient matrix method to calculate static displacement field of a dislocation source in a stratified half space, *Chin. J. Geophys.* **32,** 191–205.

Xu, C., Y. Liu, Y. Wen, and R. Wang (2010). Coseismic slip distribution of the 2008 M_w 7.9 Wenchuan earthquake from joint inversion of GPS and InSAR data, *Bull. Seismol. Soc. Am.* **100,** 2736–2749.

Xu, X., X. Wen, G. Yu, G. Chen, Y. Klinger, J. Hubbard, and J. Shaw (2009). Coseismic reverse- and oblique-slip surface faulting generated by the 2008 M_w 7.9 Wenchuan earthquake, China, *Geol. Soc. Am.* **37,** 515–518.

Yu, G., X. Xu, Y. Klinger, G. Diao, G. Chen, X. Feng, C. Li, A. Zhu, R. Yuan, T. Guo, X. Sun, X. Tan, and Y. An (2010). Fault-scarp features and cascading-rupture model for the M_w 7.9 Wenchuan earthquake, eastern Tibetan Plateau, China, *Bull. Seismol. Soc. Am.* **100,** 2590–2614.

Zhang, H., and Z. Ge (2010). Tracking the rupture of the 2008 Wenchuan earthquake by using the relative back-projection method, *Bull. Seismol. Soc. Am.* **100,** 2551–2560.

Zhu, A., X. Xu, G. Diao, J. Sun, X. Feng, Q. Sun, and Y. Wang (2008). Relocation of the M_S 8.0 Wenchuan earthquake sequence in part: Preliminary seismotectonic analysis, *Seismol. Geol.* **30,** no. 3, 759–767 (in Chinese).

Zhu, L., and L. A. Rivera (2002). A note on the dynamic and static displacements from a point source in multilayered media, *Geophys. J. Int.* **148,** 619–627.

U.S. Geological Survey
Denver Federal Center
MS 966 Box 25046
Denver, Colorado 80225
(S.H., Y.Z.)

Centro de Geociencias
Universidad Nacional Autonoma de Mexico
Campus Juriquilla
Queretaro, Mexico
(C.M.)

Instituto de Ingenieria, UNAM
Edificio 1 Cubiculo 108
Ciudad Universitaria, Coyoacan
Mexico D.F., C.P. 04510
(L.R-G.)

U.S. Geological Survey
MS 977, 345 Middlefield Ave.
Menlo Park, California 94025
(W.M.)

Manuscript received 27 March 2012